Sampling and Processing for Compressive Holography[◊]

Sehoon Lim, Daniel L. Marks, and David J. Brady*

Duke University Fitzpatrick Center for Photonics and Communications Systems, Durham, North Carolina 27705, USA

**Corresponding author: dbrady@duke.edu*

Compressive holography applies sparsity priors to data acquired by digital holography to infer a small number of object features or basis vectors from a slightly larger number of discrete measurements. Compressive holography may be applied to reconstruct 3D images from 2D measurements or to reconstruct 2D images from sparse apertures. This paper is a tutorial covering practical compressive holography procedures including field propagation, reference filtering, and inverse problems in compressive holography. We present as examples 3D tomography from a 2D hologram, 2D image reconstruction from a sparse aperture and diffuse object estimation from diverse speckle realizations.

OCIS codes: 0900.1995, 100.6950, 110.1758, 110.6150.

[◊]Datasets associated with this article are available at http://midas.osa.org/midaspre/item/view/1034. Links such as "View 1" that appear in figure captions and elsewhere will launch custom data views if ISP software is present.

1. Introduction

Digital holography is the capture of coherent fields scattered from objects on electronic photometric sensors [1]. These holograms may yield information about these objects including shape, reflectivity, and acoustic or mechanical deflections. Digital processing allows an almost unlimited flexibility to process sampled holographic data to discern features. Recently, the method of compressive sensing [2, 3] has been developed to determine the complex features of objects using relatively few measurements. Rather that assume that objects may contain arbitrary features, most of which are unlikely to occur, compressive sensing imposes *a priori* constraints on the object that assume it possesses only a small number of a large set of predefined features, and the identity of these features is inferred from the data. Many

objects of interest in holography are of such a type, including three-dimensional objects which may be largely contiguous and also possess much empty space, and two-dimensional images which may have large contiguous regions. Compressive holography advantageously combines compressive sensing with digital holography so that two-dimensional holograms or sparse aperture holograms may be used to infer object properties that would be otherwise undetermined.

Applying compressive and feature-specific priors to optical imaging is an area of increasingly intensive study. Numerous designs for feature specific [4] and compressive [5] optical imagers have been developed over the past decade. Several studies have extended these approaches to digital holography. Zhang *et al.* used linear [6] and nonlinear [7] inverse algorithms to reconstruct sections of 3D images. Our group has completed several studies of compressive holographic tomography [8,9], millimeter wave holography [10] and diffuse holography [11]. Denis *et al.* have also applied sparsity constraints in holographic imaging [12]. Fournier *et al.* theoretically estimated single point resolution in compressive holographic tomography [13]. Marim *et al.* decompressively reconstructed a 2D microscopic image with fewer measurements [14,15]. Rivenson *et al.* suggested variable sub-sampling scheme for compressive Fresnel holography [16], and demonstrated compressive measurement for multiple view projection incoherent holography [17]. Xu *et al.* adopted the compressive holographic tomography technique [8] to filter the object signal in inline coherent anti-Stokes Raman scattering holography [18]. Xu *et al.* effectively reduced the number of measurements in THz imaging [19]. In a broader scope, Coskun *et al.* compressively decoded sparse objects' distribution in lensless wide-field fluorescent imaging [20]. Suzen *et al.* used sparsifying basis to improve reconstructions with under-sampled data in diffuse optical tomography [21]. Given that both computational imaging and compressive sensing are rapidly evolving, it is certain that great advances for these fields are to come.

The common themes of this previous work are first, that image estimation using sparsity priors is useful in holography and second, that co-design of nonlinear estimators with sampling strategies and geometries may yield significant improvements. While these basic themes may be applied to a very wide diversity of holographic systems, the basic advantage that they convey are summarized by the idea that compressive measurement delivers more signal values with fewer measurements. For this advantage to have value, one must assume a cost or feasibility model that inhibits complete measurement. The simplest such models arise in 3D estimation from 2D data, in which case complete sampling is not physically possible in a single time step, and 2D or 3D estimation from sparse apertures, in which case complete sampling is not economically desirable.

This paper reprises a tutorial presentation on compressive holography at the 2011 Optical Society of America topical meeting on Digital Holography. Our goal is to describe basic

mathematical tools for decompressive analysis and reconstruction of holographic data. To aid the reader, we have uploaded Matlab codes for the procedures described. Given that compressive holography may be particularly effective in reconstruction of high pixel count images, we pay particular attention to digital propagation of fields with large numbers of samples in Section 3. We then turn to holographic image processing in Section 4. Holographic image processing differs from radar and other coherent imaging systems only in the need to filter the signal from the reference in isolating the coherent field from irradiance data. Traditionally, this isolation is done by putting the holographic signal on a spatial or temporal sideband [22]. As demonstrated in Section 4, however, constrained nonlinear estimators can isolate the holographic image from reference and background from in-line holographic data. Following the coherent image estimation method, we present a simulation of compressive holography on 3D object reconstruction from 2D holograms in Section 5.

Incoherent image estimation is discussed because if the scattering phase is random (e.g. if speckle is present) then holographic images may not be sparse in the conventional compressive sensing sense. However, the underlying scattering amplitude (e.g. the incoherent image) is generally sparse. The method described in Section 6 enables decompressive estimation of incoherent images from digital holographic data. In last two sections, we present simulations of compressive holographic reconstruction of diffuse objects. Section 7 describes 3D tomography for diffuse objects, imposing sparsity constraints on the incoherent image. Finally, Section 8 describes image reconstruction from sparse aperture holograms. Since the incoherent image estimation takes advantage of expanded modulation transfer function (MTF) support, the method mitigates the incomplete measurements of sparse aperture. We begin this agenda by briefly explaining the procedure of compressive holography in terms of compressive sensing and digital holography.

2. The Procedure of Compressive Holography

To apply compressive sensing to digital holography, one must first determine the features in the object that are likely to be present so that compressive inference methods may be applied. The object vector which describes these features to be reconstructed is expressed as a linear sum of a generally linearly dependent set of dictionary vectors. A sparse reconstruction of the object means that only a small number of these dictionary vectors are used for any given reconstruction of an object. Examples of the dictionary vectors include the canonical basis for groups of point-like objects, total variation (TV) constraints for objects with few edges and large uniform regions, wavelet bases, and the Fourier basis. There are restrictions about the "coherence" [23] between the measurements and the object basis that limit the fidelity of the reconstructions, namely, whether or not the correct dictionary elements are inferred to be present in the object vector.

A digital holography setup typically comprises these parts: a source of coherent light such as a laser, an object to test, and an electronic photometric sensor. Light is scattered from the object to test and falls on the sensor plane. Often an interferometer such as a Michelson or Mach-Zehnder setup is used to create a reference beam to be interfered on the sensor. Typical geometries used for digital holography include Gabor in-line holography and Leith-Upatnieks (LU) off-axis holography. Because only the intensity of the interference between the reference and object-scattered fields is measured, there is an ambiguity in the object field often called the conjugate field or image. The choice of geometry is often dictated by the acceptable ambiguity.

One or more holograms may be acquired, perhaps moving the object or sensor between each acquisition. This data is processed to produce a reconstruction of the object using a given dictionary. Determining which dictionary elements and the magnitudes of their weights is typically achieved by basis pursuit or ℓ_1 minimization with a least-squares fit to the data. There are many algorithms for solving basis pursuit and ℓ_1 minimization problems. For example, TwIST is applied in much of the work detailed here because of its flexibility and simplicity. To apply these algorithms, a numerical simulation of the hologram formation process is used so that the data may be fit to successive candidate objects. This simulation usually includes a means of digital propagation that models the diffraction of fields through space. Digital holography differs from radar in that the transverse scale of these fields may span $10^3 - 10^5$ wavelengths. Because of the computation and storage required to propagate wide area fields often encountered in compressive holography, we have included details on this step.

3. Field Propagation

Digital holography numerically backpropagates the scattered field by using a field propagation model [24]. Because the propagation is performed in discrete domain, the field propagation model must sample the field at a rate to avoid aliasing, yet not overly increase computational and storage costs. In general the propagated object field is given by the Rayleigh-Sommerfeld diffraction formula [25]. Under the paraxial approximation in optics, the object field is simplified to the model of Fresnel approximation method (FAM),

$$E_o(x,y) \;\; = \frac{ke^{jkz}}{j2\pi z} e^{j\frac{k}{2z}(x^2+y^2)} \iint dudv e^{-j\frac{k}{2z}(2xu+2yv)} E_s(u,v) e^{j\frac{k}{2z}(u^2+v^2)}, \tag{1}$$

where spatial coordinates (x, y) and (u, v) respectively indicate the object plane and the detector plane. Note that k is the wavenumber, λ is the wavelength, and z is the propagation distance in the optical axis.

In the discrete measurement, the pixel resolution δx and the field of view (FOV) Δx are

expressed by [26]

$$\delta x = \frac{\lambda z}{N \delta u}, \tag{2}$$

$$\Delta x = \frac{\lambda z}{\delta u}, \tag{3}$$

where N is the number of detector pixels. δx and Δx follow the Fourier relationship between the object domain x and the detection domain u. They are functions of a scaling factor λz so the propagation distance z is a critical parameter to consider for processing design. The computational simplicity of FAM arises in that the FAM uses a single 2D Fourier transform for backpropagation. Note that the validity of FAM is only guaranteed for paraxial imaging.

The angular spectrum method (ASM) has a different analytical derivation without any approximation. The object field $E_o(u, v)$ is considered as a 2D convolution of the scattered field $E_s(x, y)$ and a backpropagation kernel. By using the convolution theorem in Fourier analysis, the ASM is

$$E_o(x, y) = \frac{1}{(2\pi)^2} \iint du\, dv\; e^{-j(k_u u + k_v v)} E_s(u, v) \iint dk_u\, dk_v\; e^{jz\sqrt{k^2 - k_u^2 - k_v^2}} e^{j(k_u x + k_v y)}, \tag{4}$$

where the term $e^{jz\sqrt{k^2 - k_u^2 - k_v^2}}$ is the transfer function that is Fourier transformed from the point spread function [27].

Due to the difference of analytical forms, the ASM has the different pixel resolution and FOV [28].

$$\delta x = \delta u, \tag{5}$$

$$\Delta x = N \delta u, \tag{6}$$

where δx and Δx of ASM are independent to the propagation distance z, different from those of FAM. The computational complication of ASM happens due to the two 2D Fourier transforms for backpropagation. Compared to the FAM, the computational size increases linearly proportional to z because the ASM does not have the scaling factor. Thus, the ASM is theoretically more accurate than the FAM. However, its computational load is problematic in far field imaging.

To overcome the storage and computational burdens of ASM but preserve its accuracy, we propose the Fresnel Scaled Angular Spectrum Method (FSASM). The propagated field, as in the FAM, is expressed as $E_o(x, y) = S(x, y) \frac{k e^{jkz}}{j 2\pi z} e^{j \frac{k}{2z}(x^2 + y^2)}$, with $S(x, y)$ being a slowly-varying function multiplied by a spherical wave. This may be substituted into Eq. (4) and the order of integration changed:

$$\begin{aligned} S(x, y) = \frac{jz e^{-jkz}}{2\pi k} \iint du\, dv\; e^{-j(k_u u + k_v v)} E_s(u, v) \\ \iint dk_u\, dk_v\; e^{jz\sqrt{k^2 - k_u^2 - k_v^2}} e^{j(k_u x + k_v y)} e^{-j \frac{k}{2z}(x^2 + y^2)}. \end{aligned} \tag{7}$$

We define $\tilde{S}(k_x,k_y)=\iint dx\,dy\,e^{-j(k_x x+k_y y)}S(x,y)$ and insert it to find

$$\begin{aligned}\tilde{S}(k_x,k_y)=&\tfrac{jze^{-jkz}}{2\pi k}\iint du\,dv\;e^{-j(k_u u+k_v v)}E_s(u,v)\\&\iint dk_u\,dk_v\;e^{jz\sqrt{k^2-k_u^2-k_v^2}}\iint dx\,dy\,e^{-j(k_x x+k_y y)}e^{j(k_u x+k_v y)}e^{-j\frac{k}{2z}(x^2+y^2)}.\end{aligned}\tag{8}$$

The inner integral is evaluated as

$$\begin{aligned}\tilde{S}(k_x,k_y)=&\tfrac{jze^{-jkz}}{2\pi k}\iint du\,dv\;e^{-j(k_u u+k_v v)}E_s(u,v)\\&\iint dk_u\,dk_v\;e^{jz\sqrt{k^2-k_u^2-k_v^2}}\left[\tfrac{-2\pi jz}{k}e^{j\frac{z}{2k}\left[(k_u-k_x)^2+(k_v-k_y)^2\right]}\right].\end{aligned}\tag{9}$$

To continue, we separate the exponential kernel $e^{jz\sqrt{k^2-k_u^2-k_v^2}}=e^{jzR(k_u,k_v)}e^{jkz}e^{-j\frac{z}{2k}(k_u^2+k_v^2)}$ with $R(k_u,k_v)=\sqrt{k^2-k_u^2-k_v^2}-k+(k_u^2+k_v^2)/2k$. This transforms the convolution integral into two successive convolutions, one of which applies the fourth and higher-order terms of the angular spectrum kernel, and the second of which applies the second-order Fresnel diffraction term which is implemented by the conventional FAM. The FSASM is a modified FAM which pre-corrects the FAM for the fourth-order and higher terms missing from the FAM before applying the FAM. Inserting this separated kernel and cancelling terms, the result is

$$\begin{aligned}\tilde{S}(k_x,k_y)=&\tfrac{z^2}{k^2}e^{j\frac{z}{2k}(k_x^2+k_y^2)}\iint du\,dv\;e^{-j(k_u u+k_v v)}E_s(u,v)\\&\iint dk_u\,dk_v\;e^{jzR(k_u,k_v)}e^{-j\frac{z}{k}(k_u k_x+k_v k_y)}.\end{aligned}\tag{10}$$

Reinserting $E_o(x,y)$ and rearranging again, the result is

$$\begin{aligned}&E_o(x,y)=\tfrac{ze^{jkz}}{j(2\pi)k}e^{j\frac{k}{2z}(x^2+y^2)}\iint dk_x\,dk_y\;\;e^{j(k_x x+k_y y)}e^{j\frac{z}{2k}(k_x^2+k_y^2)}D(k_x,k_y),\\&\text{with}\\&D(k_x,k_y)=\tfrac{1}{(2\pi)^2}\iint dk_u\,dk_v\;e^{-j\frac{k_u z}{k}k_x-j\frac{k_v z}{k}k_y}e^{jzR(k_u,k_v)}\left[\iint du'\,dv'\;e^{-j(k_u u'+k_v v')}E_s(u',v')\right].\end{aligned}\tag{11}$$

To transfrom the outer integral into a Fresnel diffraction integral, we substitute $u=-\frac{k_x z}{k}$ and $v=-\frac{k_y z}{k}$:

$$\begin{aligned}&E_o(x,y)=\tfrac{ke^{jkz}}{j2\pi z}e^{j\frac{k}{2z}(x^2+y^2)}\iint dk_x\,dk_y\,e^{-j\frac{k}{z}(ux+vy)}e^{j\frac{k}{2z}(u^2+v^2)}D(u,v),\\&\text{with}\\&D(u,v)=\tfrac{1}{(2\pi)^2}\iint dk_u\,dk_v\;e^{j(k_u u+k_v v)}e^{jzR(k_u,k_v)}\left[\iint du'\,dv'\;e^{-j(k_u u'+k_v v')}E_s(u',v')\right].\end{aligned}\tag{12}$$

This is the desired result. Note that no approximations have been made from deriving the FSASM from the ASM. The diffraction calculation has been divided into two parts. The first part is to calculate the field $D(u,v)$ that is corrected for fourth-order and higher terms of the diffraction kernel. As shown above, this is accomplished using the ASM in the calculation of $D(u,v)$ with the kernel $e^{jzR(k_u,k_v)}$ rather than $e^{jz\sqrt{k^2-k_u^2-k_v^2}}$. The second step is to apply the FAM to the corrected data $D(u,v)$ in the calculation of $E_o(x,y)$. This allows the rescaling inherent to the FAM so that the sampling rate may be increased and therefore the computational burden decreased.

The limitation of the FSASM is that the convolution in the calculation of $D(u,v)$ increases the support of $D(u,v)$ relative to $E_s(u,v)$ increasing N in Eq. (2) and therefore a smaller sampling rate δx is required. The sampling of the kernel $e^{jzR(k_u,k_v)}$ in the frequency domain is aliased for a sufficiently large z unless the support of $D(u,v)$ is increased. If the support of $D(u,v)$ is permitted only to double compared to $E_s(u,v)$ so that δx is halved, then $z < \frac{2N\delta u^4}{\lambda^3}$. In practice this estimate, like the conditions governing the use of the FAM, may be overly stringent as the higher-order oscillatory terms tend to cancel more readily. While the FSASM is exact, its computational burden may become overly great with large z as the ASM does. Unlike the ASM, the limitation ultimately lies in the approximation of the rapidly-varying component of the field, the spherical wave, by a quadratic approximation given by the FAM.

Both the ASM and the FSASM are compared by using off-axis hologram data in Fig. 1. A point object was experimentally interfered by a spherical reference field at 2 m range. Fig. 1(a) shows 200 × 200 pixel image from original 1944 × 1944 pixel image for the phase of object scattered field. We propagate the scattered field back to the object plane by using two propagation methods. Fig. 1(b) shows 1944 × 1944 pixel image for the backpropagation with the ASM. The point object occupies approximately 135 pixels in diameter by using the FWHM criterion. Since the pixel resolution is equivalent to the pixel pitch in the ASM, Eq. (6), the point size is estimated to 297 μm approximately. Fig. 1(b) shows 29 × 29 pixel image for the backpropagation with the FSASM. Since the Fresnel scaling factor is applied to the FSASM, the pixel resolution is 296 μm corresponding to the object size of the ASM. For a given aperture size, the effective pixel resolution is determined by the Fraunhofer formular [25]. Thus, the FSASM does not suffer from the upsampled data unlike the ASM. The FSASM achieves 575.4 mm FOV, however, the ASM does only 4.3 mm due to the upsampled resolution.

4. Reconstruction of Compressive Holograms

This section presents the mathematical model for holographic tomography. To be able to apply linear field propagation models such as the FAM, ASM, and FSASM, one must determine the fields to be propagated from the intensity of the holograms. In the reconstruction process, algorithmic filtering replaces the conventional holographic methods. The hologram intensity $I(u,v)$ is expressed by interfering scattered field $E_s(u,v)$ and reference field $R(u,v)$.

$$I(u,v) = |R(u,v) + E_s(u,v)|^2, \tag{13}$$

$$= |R(u,v)|^2 + |E_s(u,v)|^2 + R^*(u,v)E_s(u,v) + R(u,v)E_s^*(u,v), \tag{14}$$

where the superscript '*' denotes a complex conjugate and (u,v) indicates the spatial coordinates. The squared field term $|E_s(u,v)|^2$ produces the autocorrelation term in the Fourier

domain. The conjugate term $R(u,v)E_s^*(u,v)$ also produces the twin image in the reconstruction.

Gabor holography possesses an ambiguity due to the squared-field term and the conjugate term due to the in-line geometry [29]. If the object is known to be far from the sensor plane, this ambiguity can be partially removed by filtering the scattered field axially to remove the conjugate and squared-field terms. In Gabor holography, the term $|R(u,v)|^2$ is simply a constant, hence the effect of $|R(u,v)|^2$ can be removed by eliminating the constant term at the origin in the Fourier transform of the interference irradiance measurements $I(u,v)$. Since we simply assume $R(u,v)$ is 1, we may proceed with $R^*(u,v)E_s(u,v) + R(u,v)E_s^*(u,v) + |E_s(u,v)|^2 = 2\mathrm{Re}\{E_s(u,v)\} + |E_s(u,v)|^2 = 2\mathrm{Re}\{E_s(u,v)\} + e(u,v)$.

The scattered field E_s is defined under the Born approximation as

$$E_s(u,v) = \iiint dxdydz\eta(x,y,z)h(u-x,v-y,z), \tag{15}$$

where h is the point spread function [27] and η is the scattering potential of 3D object. Note the sample spacings are $\Delta_x = \Delta_y = \Delta$ and the sampling pitch is Δ_z in the z-axis. Also, the number of pixels along each dimension of the detector is N. The discrete model of scattered field can be expressed by using the ASM,

$$E_{n_1n_2} = \mathcal{F}_{2D}^{-1}\left\{\sum_l \hat{\eta}_{m_1m_2l} e^{ikl\Delta_z} e^{il\Delta_z\sqrt{k^2-m_1^2\Delta_k^2-m_2^2\Delta_k^2}}\right\}, \tag{16}$$

where $e^{ikl\Delta_z}$ indicates the phase delay of individual slices in the 3D datacube and $\hat{\eta}_{m_1m_2l}$ is the Fourier transform of discrete scattering potential $\eta_{m_1m_2l} = \eta(m_1\Delta, m_2\Delta, l\Delta_z)$.

A linear transformation of the holographic measurement is expressed by using Eq. (16),

$$\bar{g} = G_{2D}QBf, \tag{17}$$

where $B = \mathrm{bldiag}(F_{2D}, F_{2D}, \cdots, F_{2D})$ with F_{2D} being the matrix representing the 2D DFT whose size is $(N_x \times N_y) \times (N_x \times N_y)$ and "bldiag" denoting the block diagonal matrix, $Q = [P_1P_2\cdots P_{N_z}]$ with $[P_l]_{m_1m_2} = e^{ikl\Delta_z}e^{il\Delta_z\sqrt{k^2-m_1^2\Delta_k^2-m_2^2\Delta_k^2}}$; $[P_l]_{m_1m_2}$ represents the element of the matrix P_l at the intersection of the row m_1 and the column m_2, and G_{2D} represents the 2D inverse DFT matrix. The Gabor hologram measurement may be simplified by

$$g = 2\mathrm{Re}\{\bar{g}\} = 2\mathrm{Re}\{G_{2D}QBf\} = 2\mathrm{Re}\{Hf\} + e + n, \tag{18}$$

where $g \in \mathbb{R}^{N_x \times N_y}$ represents the Gabor hologram from which the constant term is removed, and e and n denote vectorized $|E(x,y)|^2$ and additive noise, respectively.

The nonlinear term e is filtered in the measurement plane since the reconstruction algorithm propagates only diffraction patterns. The conjugate term is also filtered by confining

the estimation to only the one side of the measurement plane (i.e., $z \geq 0$). In this manner, we may effectively isolate most of the errors that result from the Gabor hologram.

The linear transformation model, Eq. (18), is inverted by decompressive inference by either selecting a basis, typically a particular wavelet basis, on which f may be assumed to be sparse or by enforcing a sparsity constraint on the total variation, as defined by Rudin *et al.* [30], of f. We choose the second approach here and estimate f as

$$\hat{f} = \arg\min_{f} ||f||_{TV} \text{ such that } g = Hf, \tag{19}$$

where $\|f\|_{TV}$ is defined by

$$\|f_k\|_{TV} = \sum_{k} \sum_{n_1} \sum_{n_2} |\nabla(f_k)_{n_1,n_2}|, \tag{20}$$

where f_k denotes a 2D plane of the 3D object datacube. We adapt the two-step iterative shrinkage/thresholding algorithm (TwIST) [31] to solve this optimization problem.

5. Holographic Tomography

As a first example of compressive holography, we consider single shot holographic tomography by using the reconstruction model of Section 4. While the volume reconstruction from a single 2D hologram is ill-posed, this problem can be solved by imposing sparsity constraints on the reconstructed volume. With the total variation constraints, structure is localized in space because the total variation is minimized when the fewest edges are present in the reconstruction.

The simulation code (e.g. a demo file, "mainHoloTomo.m", and supplemental files, "Functions") is composed of six functional blocks as presented in the uploaded files. In the Parameters block, a Gabor holographic measurement is designed at a wavelength of 0.633 μm. We generate a 3D datacube composed of $64 \times 64 \times 5$ pixels in the object space. The pixel pitch is designed considering the the aliasing analysis in the appendix. The maximum phase variation of the angular spectrum is less than π, using Eq. (33) with a pixel pitch of 30 μm. The effective aperture size of the hologram measurement is determined by the size of the object features, so the space resolutions are given by $\Delta_x \approx w$ and $\Delta_z \approx 4w^2/\lambda$ [8]. Assuming a cross section of about 2 pixels (e.g. 60 μm), the axial resolution achieves about 23 mm in reconstruction.

In the Object Generation block, 2D objects such as alphabet letters are axially distributed as shown in Fig. 2(a). Note the axial coordinate goes from the left ($z = 0$) to the right ($z = 92mm$) and the first object plane ($z = 0$) is the measurement plane. In the Propagation Kernel block, angular spectrums for individual slices are defined depending on the propagation distances. Since this simulation is performed in near-field imaging, the ASM,

Eq. (16), numerically propagates the object field to the measurement plane. We use a plane wave for the object illumination, thus, the illumination field is simply set to one. Fig. 2(b) shows phases of the propagation kernels in the datacube.

In the Field Measurement and Backpropagation block, propagated fields are linearly summed in the measurement plane as shown in Fig. 2(c). To demonstrate algorithmic field filtering, the squared fields e, Eq. (18) of objects are added to the propagated fields. Then, the measurement fields are propagated back to the original object planes by using adjoint propagation kernels. The backpropagation of a Gabor hologram is an ill-conditioned inverse problem so the individual slices suffer from out-of-focus images from the other slices in Fig. 2(d).

In the Propagation Operator block, we define forward and backward propagation operators. Here the backward propagation is the adjoint operation of the forward propagation. Since Gabor holography generates only real values in Eq. (18), both propagations take only real values of propagated fields in the measurement plane.

In the TwIST Algorithm block, the object estimate is iteratively updated under sparse constraint on TV basis. The TwIST algorithm is composed of a least square minimization term and a TV based denoising term, which are regularized by the parameter τ. Also, the number of iterations is a critical parameter to stably converge to the solution. Since the TV based denoising term is not defined in complex domain, the real and imaginary parts are independently processed in a vectorized form. The vectorized data of measured fields are plugged into the linear inverse model of iterative method. Fig. 2(e) shows the decompressive reconstruction using the TwIST algorithm. The decompressive reconstruction is superior to the backpropagation since the out-of-focus images are effectively removed. The object field is filtered in 3D object space by splitting the squared field in the measurement plane. This reconstruction model can be applied to single shot tomography by replacing the measured fields with a real Gabor measurement.

6. Holographic Data Process of Diffuse Objects

This section describes the incoherent image estimation model to allow holographic tomography of a diffuse object with speckle suppression. Incoherent image estimation using multiple speckled realizations effectively retrieves the smooth features destroyed by speckle effects. The field randomness, caused by speckle, degrades image resolution of the reconstructed fields [11]. Since the sparsity constraint is imposed on smooth features of incoherent scattering density α, we decompressively reconstruct the scattering density with fewer measurements.

The high sensitivity of LU holography enables compressive holography for weak scattering of diffuse objects [15]. In LU holography, off-axis geometry is used to make a linear phase reference field $R = e^{j\alpha u}$, where α is angular frequency [22]. The object-scattered field is sepa-

rated from the other terms in the Fourier domain thanks to the linear phase term. Applying Fourier filtering to Eq. (15), the scattered field term $R^*(u,v)E_s(u,v)$ can be extracted.

The scattered field is also defined by the Born approximation and the ASM in the same manner with Section 4. After Fourier filtering, the holographic measurement has complex field values without the squared term and the conjugate term. Then, the k-th holographic measurement g_k can be written by,

$$g_k = Hf_k + w_k, \tag{21}$$

where $g_k \in \mathbb{C}^{M\times 1}$ with $M = N_x \times N_y$ and w_k indicates independent additive Gaussian noise.

For fully developed speckles, the 3D scattered field $f = [f_1\ f_2\ \cdots\ f_N]^T$ with $N = N_x \times N_y \times N_z$, has the complex circular Gaussian probability density [32]:

$$p(f) = \frac{1}{\pi^N \det(R_f)} \exp\left(-f^H {R_f}^{-1} f\right), \tag{22}$$

where $\mathrm{E}[f] = 0$, $R_f = \mathrm{E}[ff^H] = \mathrm{diag}(\mathrm{E}[|f_1|^2], \mathrm{E}[|f_2|^2], \cdots, \mathrm{E}[|f_N|^2]) = \mathrm{diag}(\alpha_1, \alpha_2, \cdots, \alpha_N) = \mathrm{diag}(\alpha)$. Symbolically, we write $f \sim CN(0, R_f)$. The covariance W is defined by $\sigma^2 I$ with I denoting the $M \times M$ identity matrix. This statistical model implies that g has also a complex Gaussian probability density with zero mean and covariance R_g: $g \sim CN(0, R_g)$, with $R_g = HR_fH^H + \sigma^2 I = H\left(R_f + \sigma^2 I\right)H^H$.

Since $HH^H = I$, the minimum-norm solution [33] to the inverse problem in Eq. (21) is given by

$$\hat{f}_k = H^H\left(HH^H\right)^{-1} g_k = H^H g_k = H^H H f_k + H^H w_k, \tag{23}$$

from which an estimate of the incoherent image of the scattering field (e.g. the diagonal elements of R_f) can be formed as

$$\hat{s}_n = \frac{1}{K}\sum_{k=1}^{K} |\hat{f}_{nk}|^2. \tag{24}$$

Let $H = [h_1\ h_2\ \cdots\ h_N]$ where h_n denotes the n-th column of H, and $[H^H H]_{mn} = \langle h_m, h_n\rangle = {h_m}^H h_n$. Thus, the expected value of the estimate $\hat{s}$ can expressed as

$$\begin{aligned} d &= \mathrm{E}[\hat{s}] \\ &= \frac{1}{K}\sum_{k=1}^{K} \mathrm{Diag}\left(E[\hat{f}_k {\hat{f}_k}^H]\right) \\ &= \mathrm{Diag}\left(E[\hat{f}\hat{f}^H]\right) \\ &= \mathrm{Diag}\left(H^H H R_f H^H H + \sigma^2 H^H H\right) \end{aligned} \tag{25}$$

where the third equality holds because the probability density of $\hat{f}_k$ is the same for all k. In particular, the fourth equality in Eq. (25) indicates that

$$E[\hat{s}_n] = \sum_{m=1}^{N} |\langle h_n, h_m \rangle|^2 \alpha_m + \sigma^2 \langle h_n, h_n \rangle = \sum_{m=1}^{N} |{h_n}^H h_m|^2 \alpha_m + \sigma^2 \|h_n\|^2, \tag{26}$$

where $\|h\|$ denotes the Euclidean norm of h. Then Eq. (26) implies that

$$d = \mathrm{E}[\hat{s}] = B\alpha + \sigma^2 W, \tag{27}$$

where d are defined as *synthetic measurements*.

Eq. (27) suggests we may solve the constrained optimization problem:

$$\alpha^* = \arg\min_{\alpha} \frac{1}{2} \|d - B\alpha\|_2^2 + \beta\Phi(\alpha). \tag{28}$$

The functional $\Phi(\alpha)$ imposes constraints on α. For decompressive inference, Φ enforces the sparsity constraints. When the incoherent scattering field is expected to have a smooth surface, we can assume that the gradient of the incoherent image is sparse. This sparsity can be incorporated by minimizing the TV of the estimate. We define TV for our problem as $\Phi(\alpha) = \|\alpha\|_{TV} = \sum_{n_x} \sum_{n_y} \sum_{n_z} |\nabla(\alpha_{n_z})_{n_x,n_y}|$.

The sparsity-constrained estimates are known to be near optimal when the columns of the system matrix form approximately an orthonormal basis [34]. To transform our system matrix to such an orthonormal basis, we apply a preconditioning method and convert $d = B\alpha + \sigma^2 W$ to $\tilde{d} = Pd = PB\alpha + \sigma^2 PW = \tilde{B}\alpha + \sigma^2 \tilde{W}$, and we solve

$$\alpha^* = \arg\min_{\alpha} \frac{1}{2} \|\tilde{d} - \tilde{B}\alpha\|_2^2 + \beta\Phi(\alpha), \tag{29}$$

instead of Eq. (28).

If B has full rank, the preconditioner P may be chosen such that $\tilde{B} = PB$ is as unitary as possible. An immediate choice of unitary $\tilde{B}$ would be the identity matrix: $\tilde{B} = I$. In this case, the preconditioner P is merely the inverse of B and the estimation problem becomes an inverse problem. However, the matrix could often be rank deficient or ill-conditioned, some nonzero singular values of B either excessively amplify the noise or cause numerical instability. To alleviate this problem, we choose P in the Tikhonov-regularized sense. That is $P = (B^H B + \lambda_t I)^{-1} B^H$, where λ_t is a Tikhonov regularization parameter. Note that λ_t suppresses or ignores a small number of singular vectors associated with numerically unstable or zero singular values.

7. Diffuse Object Tomography

As a second example of compressive holography, we consider diffuse object tomography by using the incoherent image estimation model of Section 6. The coherent image estimation

model of Section 4 cannot be used for diffuse object imaging due to speckle effects. To avoid these complications, we utilize full-developed speckled realizations to statistically obtain the incoherent scattering density. By imposing sparsity constraints on the total variation of the incoherent scattering density, incoherent structure is localized in space and the speckle is suppressed.

Processing of diffuse object tomography is again described in the processing blocks in the uploaded code (e.g. a demo file, "mainDiffuseTomo.m", and supplemental files, "MyFunctions"). In the Parameters block, we set up holographic parameters and object space. A LU hologram is taken using a coherent source at the wavelength of 0.633 μm. We generate a 3D datacube composed of $64 \times 128 \times 3$ pixels in the object space. The pixel pitch is designed to 50 μm at $\pm$ 50 mm propagation range.

In the Object Generation block, three rectangular shapes are defined axially distributing in Fig. 3(a). We design an objective lens to collect the scattered fields with an optical magnification. The center object plane is one-to-one imaged to the measurement plane at $z = 0$, and the other planes are placed in -50 mm and +50 mm ranges relative to the measurement plane. In the Propagation Kernel blocks, the ASM and the plane wave illumination are used in the same manner with holographic tomography in Section 5. Fig. 3(b) shows phases of the propagation kernels depending on the propagation distances. Since the center object plane is imaged to the measurement plane, the plane does not need a propagation phase.

In the Holographic Measurement and Backpropagation block, multiple speckled realizations support the incoherent image estimation for diffuse object tomography. Illumination randomized by multiple speckled realizations is a form of partially coherent illumination. To generate the randomized illumination, random fields are applied resulting in a complex object field. The backpropagation of a single speckled realization shows the severely degraded image in Fig. 3(c). The averaged backpropagation of multiple speckled realizations show the better image in Fig. 3(d). Nevertheless, the tomographic image is still degraded by speckles and out-of-focus images.

In the Incoherent System Matrix block, the incoherent system matrix Q is generated by Fourier transforming the squared PSF. The system matrix Q projects the original 3D object to the backpropagated image via multiple speckled realizations. The Tikhonov regularization alleviates the ill-conditioned problem in tomographic reconstruction. Using the preconditioning method in Section 6, the inverted datacube shows better tomographic image reducing the out-of-focus features in Fig. 3(e). Note the Tikhonov regularization parameter λ_t is 1.0e-08 in the reconstruction.

In the TwIST Algorithm block, forward and backward projection operators are defined. The forward projection operator D is formed by a multiplication of Tikhonov-regularized inversion of Q and Q (e.g. $pinvQ * Q$). The backward projection operator DT is an adjoint

of the forward projection operator. The averaged backpropagation is inverted using the Tikhonov-regularized inversion of the incoherent system matrix, $pinvQ$, and input to the TwIST algorithm. The TwIST algorithm is regularized by TV sparsity constraints according to Eq. (28). The parameter τ and the number of iterations are controlled to stably converge to the optimal solution. Fig. 3(f) shows the speckle suppressed image with 30 speckled realizations. Some artifacts remain in the overlapping region to the detector's perspective, due to the ambiguity of decompressive inference.

8. Sparse Aperture Holography

As a third example of compressive holography, we consider sparse aperture holography which allows high pixel count 2D imaging. Mosaics of low cost 2D sensor arrays achieve large aperture digital holography of hundreds of mega pixel fields. Scanning-based synthetic aperture holography is a method of coherent aperture synthesis. The major challenges are subaperture registration errors and the relative phase instability of the reference field to the object field due to sources such as vibration and thermal fluctuation [35].

A sparse aperture can avoid a lengthy acquisition time as well as computational compensation for the phase instabilities. Synchronization of the sensors in a sparse aperture may enable snap-shot detection eliminating phase instability. Using spatially incoherent laser illumination enables incoherent synthesis of apertures and a corresponding enhancement of MTF support [25]. Radio telescopes employ the same techniques to measure a large MTF support with a sparse aperture [36]. In addition, incoherent synthesis eliminates the speckle problems common when reconstructing diffuse objects using holography.

We compare coherent and incoherent bandpasses in a sparse aperture system with three square apertures. The MTF is obtained by the autocorrelation of the transmittance of a sparse aperture [27]. Fig. 4.(b) shows the MTF bands are located in the high frequencies, increasing the maximum frequency of the MTF. Thus, sparse aperture holography can detect higher frequency information than a single wide aperture system with equal detector area. While the loss of mid-band information can be problematic, decompressive reconstruction is used to mitigate it.

Decompressive reconstruction uses the incoherent image estimation supported by multiple speckled realizations. Decompressive inference can help mitigate the loss of some MTF support not sampled by the incoherent MTF by imposing sparsity constraints on an incoherent source or scatterer reconstruction, in a manner generalizing methods like the CLEAN algorithm. [36]

In this example, sparsity constraints on total variation decompressively localizes 2D structure alleviating the ambiguity of sparse measurement. The simulation of sparse aperture holography is mostly similar to that of diffuse object tomography in Section 7. The

codes are also uploaded for the coherent estimation (e.g. a demo file, "mainSparseCoh.m", and supplemental files, "Functions") and the incoherent estimation (e.g. a demo file, "mainSparseIncoh.m", and supplemental files, "MyFunctions"). A 2D phantom object is generated with 128×128 pixels in 2 m range as shown in Fig. 5(a). LU holography is used for lensless holographic imaging at the wavelength of 0.633 μm. The pixel pitch is assumed to be 100 μm in the measurement plane, avoiding the aliasing issue and achieving 99 μm pixel resolution in the object plane.

In the Sparse Aperture Generation block, randomized distribution of the sparse aperture maximizes decompressive inference in the measurement plane. This design follows the coherence restriction between the measurements and the object basis for the high fidelity reconstruction. In remote imaging, scattered fields have a lot of information redundancy in the measurement plane. Individual apertures are designed to be point-like detectors to reduce the measurement redundancy, and the sparse distribution of point-like apertures may be supported by a phase mask in the optical domain. Fig. 5(b) shows a sparse aperture design with a 16 percent fill factor.

In the Propagation Operators block, the FSASM is used to represent optical fields in the field range with compactness and reliability (see Section 3). Fig. 5(c) and Fig. 5(e) compare averaged backpropagations of the coherent and the incoherent image estimation. Fig. 5(e) shows high frequency features of the object because of the expanded bandpass of the incoherent image estimation. The decompressive reconstruction of incoherent image estimation, Fig. 5(d), is superior to that of coherent image estimation, Fig. 5(f), since the incoherent image estimation retains high frequency features. Fig. 5(f) shows a high quality and speckle suppressed image, although some high frequency features are lost due to the sparse and speckled measurement. Note the decompressive reconstruction was performed by the TwIST algorithm.

9. Conclusion

Three examples for compressive holography were given by following the practical procedures of compressive holography. The examples demonstrated how the compressive holography procedures utilized the co-design of non-linear estimators with sampling strategies and geometries based on object sparsity priors. The small size of the simulations allows most readers to run and understand them directly.

Since holographic measurement naturally multiplexed and compressed image data, we can demonstrate the objective of more signal values with fewer measurements. The compressive design can be effectively applied to high dimensional image estimation with high fidelity. This approach exhibits low cost and high feasibility so it will be more interested as computer processing power rapidly advances.

Appendix: Aliasing Analysis on the ASM

Aliasing in the field representation limits the performance of numerical field propagation, since discrete signal processing is generally governed by Shannon's sampling theorem. To analyze the aliasing condition under the sampling theorem, we calculate the maximum phase variation in the adjacent pixels. 1D mathematical forms are considered for the simplicity in this analysis.

In the ASM, we investigate the phase terms of the spherical field $R(u, v; z_r)$ and propagation kernel $H(f_u, f_v; z_d)$. Here we assume the hologram data is multiplied by a conjugate spherical field for far field imaging. The phase variation $\Delta\phi_R(u; z_r)$ of the spherical field $R(u; z_r)$ is calculated at the smallest increment δu

$$\Delta\phi_R(u; z_r) = \frac{2\pi}{\lambda}\left\{\sqrt{z_r^2 + (u+\delta u)^2} - \sqrt{z_r^2 + u^2}\right\}. \tag{30}$$

Using the binomial expansion with the condition that the distance z_r is larger than the aperture width u, the phase change is obtained as

$$\Delta\phi_R(u; z_r) = \frac{2\pi}{\lambda}\left\{\frac{2u\delta u + \delta u^2}{2z_r}\right\} = \frac{\pi}{\lambda z_r} 2u\delta u < \pi, \tag{31}$$

where the term δu^2 is negligible in comparison to the other term $2u\delta u$. A failure in the inequality causes aliasing, corrupting the phase information in the propagation process.

The phase variation $\Delta\phi_H(f_u; z_d)$ of the angular spectrum $H(u; z_d)$ is calculated at the smallest increment δf_u

$$\Delta\phi_H(f_u; z_d) = \frac{2\pi}{\lambda} z_d \left\{\sqrt{1 - \lambda^2(f_u + \delta f_u)^2} - \sqrt{1 - \lambda^2 f_u^2}\right\}. \tag{32}$$

Using the binomial expansion with the condition that the term $\lambda^2 f_u^2$ is less than 1, the phase change becomes

$$\Delta\phi_H(f_u; z_d) = \frac{2\pi}{\lambda} z_d \lambda^2 \left\{\frac{2f_u\delta f_u + \delta f_u^2}{2}\right\} = \pi z_d \lambda \frac{1}{\delta u}\frac{1}{\Delta u} < \pi, \tag{33}$$

where the term δf_u^2 is negligible to the term $2f_u\delta f_u$.

The accuracy of this analysis is limited by the binomial approximation, so the ASM can suffer from more aliasing than this analysis.

References

1. W. Jueptner and U. Schnars, *Digital Holography* (Springer-Verlag, New York, Berlin Heidelberg, 2005).
2. E. J. Candes, J. K. Romberg, and T. Tao, "Stable signal recovery from incomplete and inaccurate measurements," Communications on Pure and Applied Mathematics **59**, 1207–1223 (2006).

3. D. L. Donoho, "Compressed sensing," IEEE Transactions on Information Theory **52**, 1289–1306 (2006).
4. M. A. Neifeld and P. Shankar, "Feature-specific imaging," Applied Optics **42**, 3379–3389 (2003).
5. D. J. Brady, N. Pitsianis, X. Sun, and P. Potuluri, "Compressive sampling and signal inference," US patents 7283231, 7432843, 7463179, 7616306, 7463174, and 7427932, (2005).
6. X. Zhang, E. Y. Lam, and T.-C. Poon, "Reconstruction of sectional images in holography using inverse imaging," OPTICS EXPRESS **16**, 17215–17226 (2008).
7. X. Zhang and E. Y. Lam, "Edge-preserving sectional image reconstruction in optical scanning holography," JOURNAL OF THE OPTICAL SOCIETY OF AMERICA A-OPTICS IMAGE SCIENCE AND VISION **27**, 1630–1637 (2010).
8. D. J. Brady, K. Choi, D. L. Marks, R. Horisaki, and S. Lim, "Compressive holography," Opt. Express **17**, 13040–13049 (2009).
9. J. Hahn, S. Lim, K. Choi, R. Horisaki, and D. J. Brady, "Video-rate compressive holographic microscopic tomography," Opt. Express **19**, 7289–7298 (2011).
10. C. F. Cull, D. A. Wikner, J. N. Mait, M. Mattheiss, and D. J. Brady, "Millimeter-wave compressive holography," Appl. Opt. **49**, E67–E82 (2010).
11. K. Choi, R. Horisaki, J. Hahn, S. Lim, D. L. Marks, T. J. Schulz, and D. J. Brady, "Compressive holography of diffuse objects," Appl. Opt. **49**, H1–H10 (2010).
12. L. Denis, D. Lorenz, E. Thiébaut, C. Fournier, and D. Trede, "Inline hologram reconstruction with sparsity constraints," Opt. Lett. **34**, 3475–3477 (2009).
13. C. Fournier, L. Denis, and T. Fournel, "On the single point resolution of on-axis digital holography," J. Opt. Soc. Am. A **27**, 1856–1862 (2010).
14. M. M. Marim, M. Atlan, E. Angelini, and J.-C. Olivo-Marin, "Compressed sensing with off-axis frequency-shifting holography," Opt. Lett. **35**, 871–873 (2010).
15. M. Marim, E. Angelini, J.-C. Olivo-Marin, and M. Atlan, "Off-axis compressed holographic microscopy in low-light conditions," OPTICS LETTERS **36**, 79–81 (2011).
16. Y. Rivenson, A. Stern, and B. Javidi, "Compressive fresnel holography," J. Display Technol. **6**, 506–509 (2010).
17. Y. Rivenson, A. Stern, and J. Rosen, "Compressive multiple view projection incoherent holography," Opt. Express **19**, 6109–6118 (2011).
18. Q. Xu, K. Shi, H. Li, K. Choi, R. Horisaki, D. Brady, D. Psaltis, and Z. Liu, "Inline holographic coherent anti-Stokes Raman microscopy," OPTICS EXPRESS **18**, 8213–8219 (2010).
19. Z. Xu and E. Y. Lam, "Image reconstruction using spectroscopic and hyperspectral information for compressive terahertz imaging," JOURNAL OF THE OPTICAL SOCIETY

OF AMERICA A-OPTICS IMAGE SCIENCE AND VISION **27**, 1638–1646 (2010).

20. A. F. Coskun, I. Sencan, T.-W. Su, and A. Ozcan, "Lensless wide-field fluorescent imaging on a chip using compressive decoding of sparse objects," OPTICS EXPRESS **18**, 10510–10523 (2010).
21. M. Suezen, A. Giannoula, and T. Durduran, "Compressed sensing in diffuse optical tomography," OPTICS EXPRESS **18**, 23676–23690 (2010).
22. E. N. Leith and J. Upatnieks, "Reconstructed wavefronts and communication theory," J. Opt. Soc. Am. **52**, 11231130 (1962).
23. E. J. Candes and M. B. Wakin, "An introduction to compressive sampling," IEEE SIGNAL PROCESSING MAGAZINE pp. 21–30 (March 2008).
24. U. Schnars and W. Juptner, *Digital Holography, Digital Hologram Recording, Numerical Reconstruction and Related Techniques* (Springer, 2005).
25. J. W. Goodman, *Introduction to Fourier optics, 3rd Ed.* (Roberts and Company Publishers, New York, 2005).
26. U. Schnars and W. P. O. Juptner, "Digital recording and numerical reconstruction of holograms," Meas. Sci. Technol. **13**, R85–R101 (2002).
27. D. J. Brady, *Optical Imaging and Spectroscopy* (Wiley, 2009).
28. T. Kreis, M. Adams, and W. Juptner, "Methods of digital holography: A comparison," (1997), vol. 3098 of *PROCEEDINGS OF THE SOCIETY OF PHOTO-OPTICAL INSTRUMENTATION ENGINEERS (SPIE)*, pp. 224–233.
29. D. Gabor, "A new microscopic principle," Nature **161**, 777–778 (1948).
30. L. RUDIN, S. OSHER, and E. FATEMI, "NONLINEAR TOTAL VARIATION BASED NOISE REMOVAL ALGORITHMS," PHYSICA D **60**, 259–268 (1992).
31. J. M. Bioucas-Dias and M. A. T. Figueiredo, "a new twist: Two-step iterative shrinkage/thresholding algorithms for image restoration," IEEE Transactions on Image Processing **16**, 29923004 (2007).
32. J. W. Goodman, *Statistical Optics* (Wiley Inter-Science, 2000).
33. T. K. Moon and W. C. Stirling, *Mathematical Methods and Algorithms for Signal Processing* (Prentice-Hall, 2000).
34. J. Tropp, "Just relax: Convex programming methods for identifying sparse signals in noise," IEEE TRANSACTIONS ON INFORMATION THEORY **52**, 1030–1051 (2006).
35. S. Lim, K. Choi, J. Hahn, D. L. Marks, and D. J. Brady, "Image-based registration for synthetic aperture holography," Opt. Express **19**, 11716–11731 (2011).
36. A. R. Thompson, J. M. Moran, and J. G. W. Swenson, *Interferometry and Synthesis in Radio Astronomy* (Wiley, 2001).

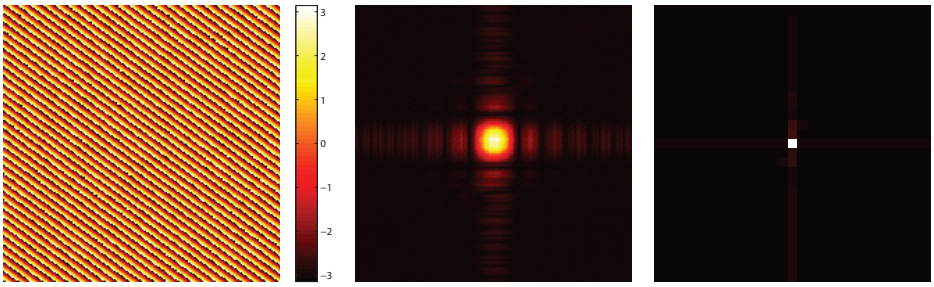

(a) (b) (c)

Fig. 1. Comparison of field propagations : (a) phase of object scattered field, (b) backpropagation w/ ASM, and (c) backpropagation w/ FSASM.

(a)

(b)

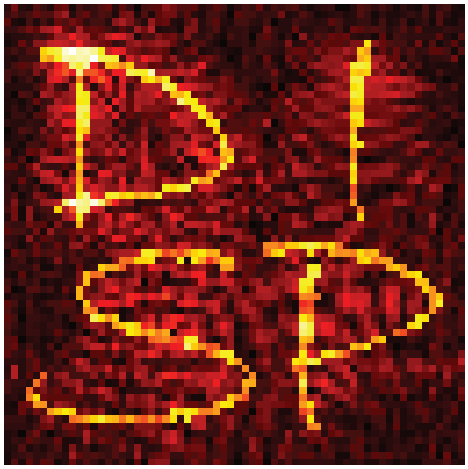

(c)

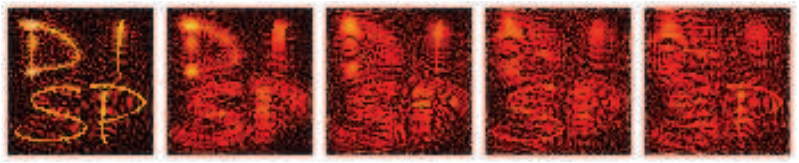

(d)

(e)

Fig. 2. Simulations for holographic tomography : (a) 3D object (View 1), (b) phase of transfer functions (View 2), (c) scattered field, (d) backpropagation (View 3), and (e) compressive reconstruction (View 4).

(a)

(b)

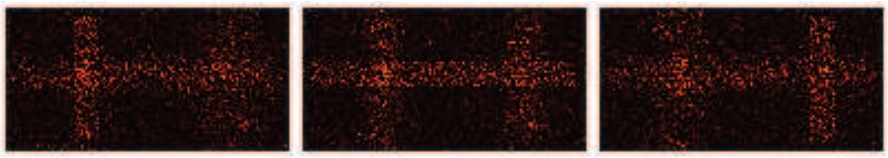

(c)

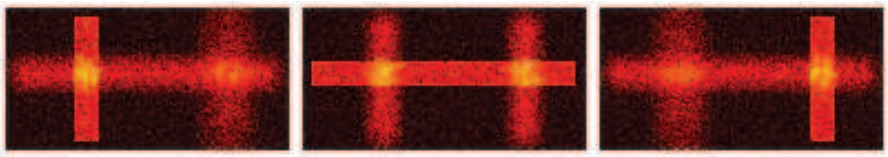

(d)

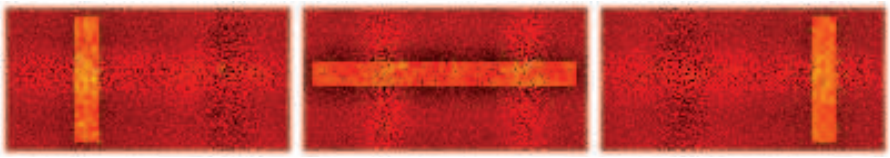

(e)

(f)

Fig. 3. Simulations for diffuse object tomography : (a) 3D object (View 5), (b) phase of propagation kernels (View 6), (c) backpropagation of single speckled realization (View 7), (d) backpropagation averaged by 30 speckled realizations (View 8), (e) backpropagation using the Tikhonov regularization w/ 30 speckled realizations (View 9), and (f) compressive reconstruction w/ 30 speckled realizations (View 10).

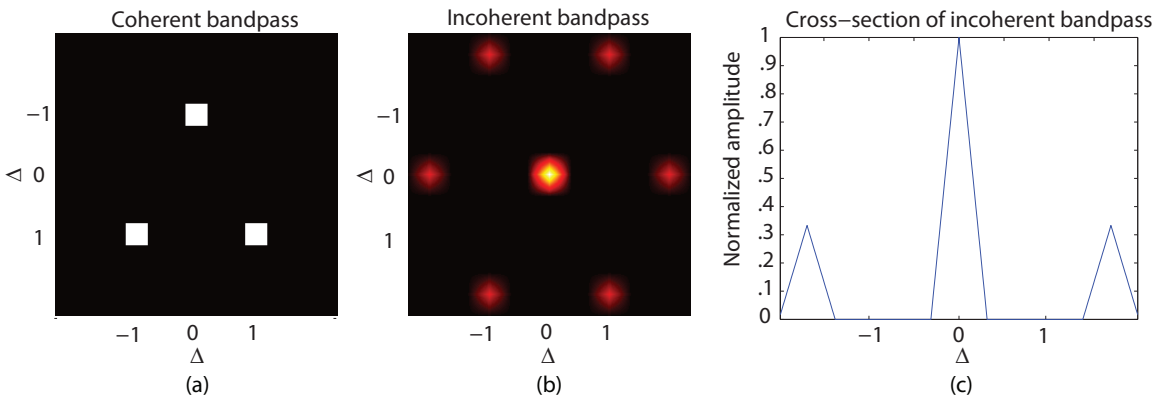

Fig. 4. Coherent and incoherent bandpasses in sparse aperture design : (a) coherent bandpass, (b) incoherent bandpass, and (c) cross-section of incoherent bandpass. Note that Δ is the space of subapertures.

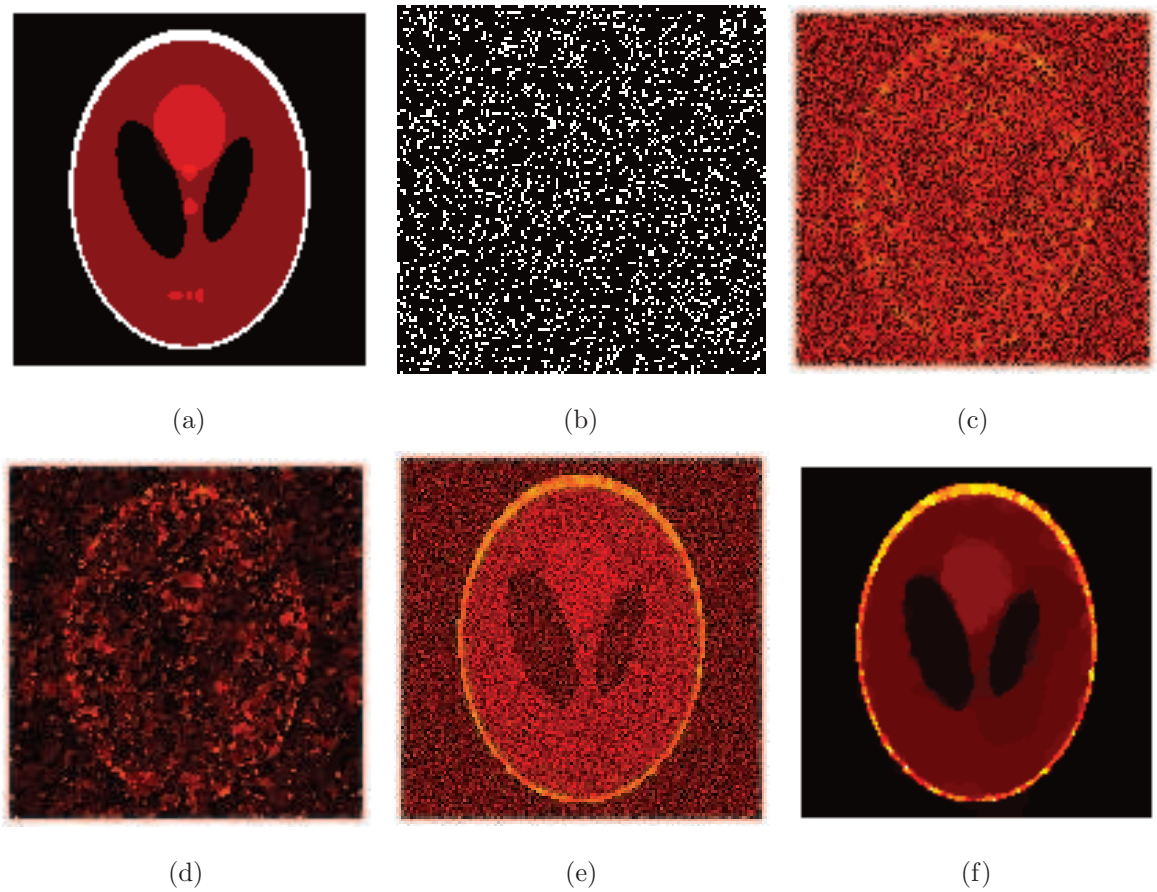

Fig. 5. Simulations for sparse aperture holography : (a) 2D object, (b) sparse aperture, (c) averaged backpropagation of coherent estimation model, (d) compressive reconstruction of coherent estimation model, (e) averaged backpropagation of incoherent estimation model, and (f) compressive reconstruction of incoherent estimation model.